In situ stress state in the Nankai accretionary wedge estimated from borehole wall failures

Chandong Chang, Lisa Mcneill, J. Casey Moore, Weiren Lin, Marianne Conin, Yasuhiro Yamada

Geochemistry Geophysics Geosystems G3

Article
Volume 11
16 December 2010
Q0AD04, doi:10.1029/2010GC003261
ISSN: 1525-2027

Published by AGU and the Geochemical Society

In situ stress state in the Nankai accretionary wedge estimated from borehole wall failures

Chandong Chang
Department of Geology, Chungnam National University, Daejeon 305-764, South Korea (cchang@cnu.ac.kr)

Lisa C. McNeill
National Oceanography Centre, Southampton, University of Southampton, Southampton SO14 3ZH, UK

J. Casey Moore
Earth and Planetary Sciences Department, University of California, Santa Cruz, California 95064, USA

Weiren Lin
Kochi Institute for Core Sample Research, JAMSTEC, Kochi 783-8502, Japan

Marianne Conin
CEREGE, Université Aix Marseille III, F-13545 Aix-en-Provence, France

Yasuhiro Yamada
Civil and Earth Resources Engineering Department, Kyoto University, Kyoto 615-8540, Japan

[1] We constrain the orientations and magnitudes of in situ stress tensors using borehole wall failures (borehole breakouts and drilling-induced tensile fractures) detected in four vertical boreholes (C0002, C0001, C0004, and C0006 from NW to SE) drilled in the Nankai accretionary wedge. The directions of the maximum horizontal principal stress (S_{Hmax}), indicated by the azimuths of borehole wall failures, are consistent in individual holes, but those in C0002 (margin-parallel S_{Hmax}) are nearly perpendicular to those in all other holes (margin-normal S_{Hmax}). Constrained stress magnitudes in C0001 and C0002, using logged breakout widths combined with empirical rock strength derived from sonic velocity, as well as the presence of the drilling-induced tensile fractures, suggest that the stress state in the shallow portion of the wedge (fore-arc basin and slope sediment formations) is predominantly in favor of normal faulting and that the stress state in the deeper accretionary prism is in favor of probable strike-slip faulting or possible reverse faulting. Thus, the stress regime appears to be divided with depth by the major geological boundaries such as unconformities or thrust faults. The margin-perpendicular tectonic stress components in the two adjacent sites, C0001 and C0002, are different, suggesting that tectonic force driven by the plate pushing of the Philippine Sea plate does not uniformly propagate. Rather, the stress field is inferred to be influenced by additional factors such as local deformation caused by gravitation-driven extension in the fore arc and thrusting and bending within individual geologic domains.

Components: 9300 words, 10 figures, 1 table.

Keywords: in situ stress; Nankai accretionary wedge; borehole breakouts; drilling-induced tensile fractures.

Index Terms: 8164 Tectonophysics: Stresses: crust and lithosphere; 8170 Tectonophysics: Subduction zone processes (1031, 3060, 3613, 8413); 3036 Marine Geology and Geophysics: Ocean drilling.

Received 21 June 2010; **Revised** 3 November 2010; **Accepted** 10 November 2010; **Published** 16 December 2010.

Chang, C., L. C. McNeill, J. C. Moore, W. Lin, M. Conin, and Y. Yamada (2010), In situ stress state in the Nankai accretionary wedge estimated from borehole wall failures, *Geochem. Geophys. Geosyst.*, *11*, Q0AD04, doi:10.1029/2010GC003261.

Theme: Mechanics, Deformation, and Hydrologic Processes at Subduction Complexes, With Emphasis on the Nankai Trough Seismogenic Zone Experiment (NanTroSEIZE) Drilling Transect
Guest Editors: D. Saffer, P. Henry, and H. Tobin

1. Introduction

[2] Knowledge of the present-day stress state in tectonically dynamic regions such as convergent plate margins is important to understand the mechanics of various geological/geophysical processes including faulting and earthquakes [*Zoback*, 1992; *Sassi and Faure*, 1996; *Suppe*, 2007]. The mechanics of accretionary wedges that lie along the convergent margin is commonly described by critical taper theory [*Davis et al.*, 1983; *Dahlen et al.*, 1984; *Zhao et al.*, 1986], which explains the geometry of the wedge, internal deformation and stress changes, and the friction along the basal detachment. *Wang and Hu* [2006] expanded the critical taper theory considering a dynamic change in stress boundary conditions associated with earthquake cycles to explain the temporal and spatial variation of stress states within the wedge. Verification of the models is often made through comparing the models with observed kinematic or mechanical boundary conditions, which can also be utilized to refine the models [e.g., *Seyferth and Henk*, 2000]. This is especially true for complicated accretionary wedge systems, where the internal deformation is inherently heterogeneous [*Kukowski et al.*, 2002].

[3] In the present study, we report our results on the state of stress in the Nankai accretionary wedge, southwest of Kii Peninsula, Japan, where the Philippine Sea plate is subducting below the Eurasian Plate. Previous efforts to determine present-day stress orientations in the Nankai region revealed diverse results depending on locations of stress indicators: margin-parallel maximum horizontal compression from earthquake focal mechanism solutions in the fore arc [*Wang and He*, 1999] and margin-normal maximum horizontal compression in the more seaward outer arc from relatively shallow borehole stress indicators [*Ienaga et al.*, 2006] and focal mechanisms of very low frequency earthquakes [*Ito et al.*, 2009]. These results suggest that the stress states in the Nankai accretionary wedge are quite complicated, presumably due to various effects such as strength of plate coupling [*Wang and Suyehiro*, 1999; *Wang*, 2000] and possibly variable deformations in different geologic domains.

[4] A recent Integrated Ocean Drilling Program (IODP) project, the Nankai Trough Seismogenic Zone Experiment (NanTroSEIZE), provides an opportunity to estimate in situ stress states, over the different geologic domains at the shallow Nankai accretionary wedge. Several vertical boreholes were drilled in the shallow portion of the wedge along a line perpendicular to the plate boundary (Figure 1) [*Tobin et al.*, 2009]. In these holes, we observed a series of drilling-induced borehole wall failures in logging-while-drilling (LWD) resistivity images of the borehole wall. These drilling-induced borehole wall failures, either in compressive (borehole breakouts) [*Bell and Gough*, 1979] or tensile (drilling-induced tensile fractures) mode [*Bell*, 1996] have been utilized to yield present-day stress information. In particular, these drilling-induced features are indicators of the in situ stress tensor, which can be used to accurately examine horizontal stress orientations and to make estimates of stress magnitudes [*Zoback*, 2007]. Approximately 20% of the World Stress Map (WSM) data were determined from such drilling-induced stress indicators [*Heidbach et al.*, 2008], and their contribution to reliable stress estimates is growing as increasing amounts of petroleum industry data are added to the WSM database [*Tingay et al.*, 2005; *Heidbach et al.*, 2010]. Such drilling-induced stress indicators were also often detected in the previous IODP boreholes drilled in the subduction margins [e.g., *Goldberg et al.*, 2003; *Ienaga et al.*, 2006; *Cook et al.*, 2008], but no previous attempts were made to constrain stress magnitudes.

[5] In this paper, we present in situ stress orientations and magnitudes constrained by these stress-induced features. We use the image logs that show borehole wall failures, as well as other mechanical parameters, either estimated or assumed, to constrain the possible

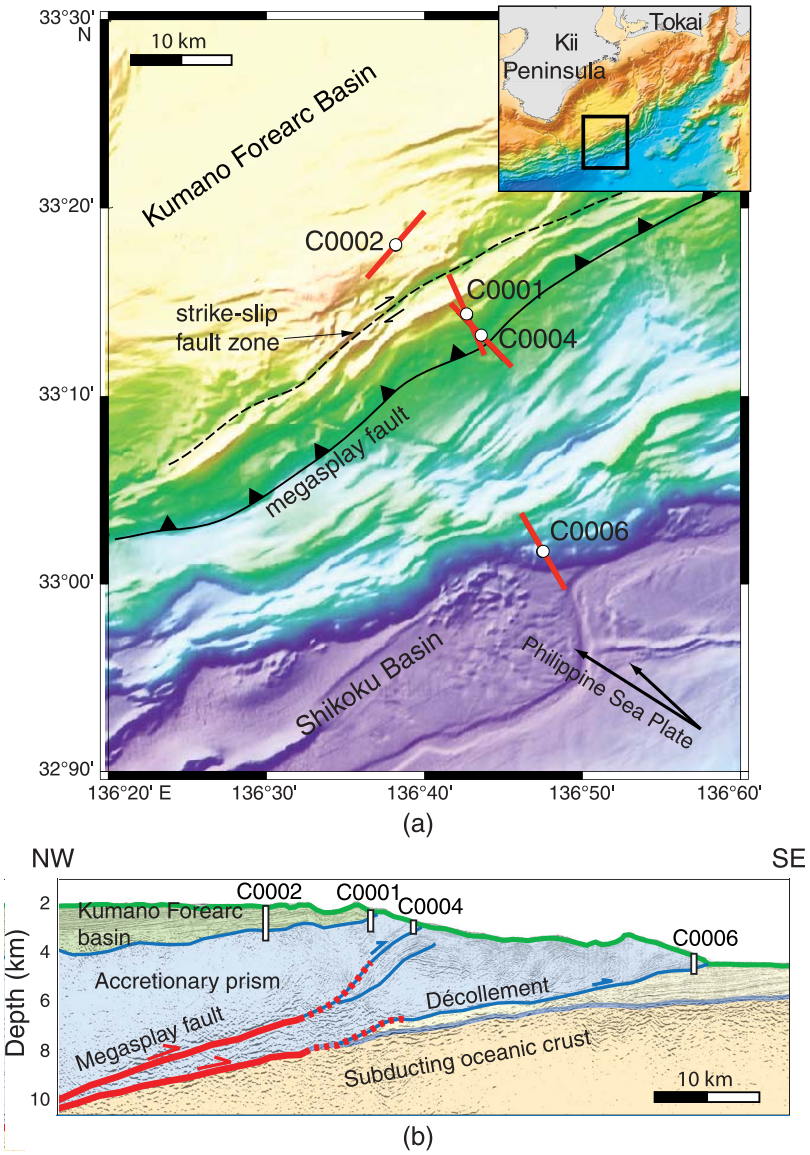

Figure 1. Study area: (a) borehole locations and the maximum horizontal stress directions determined from borehole wall failures and (b) seismic reflection profile across the subduction zone and borehole locations. Our stress orientation data for the four holes are all B ranked based on WSM quality-ranking system for image logged borehole breakouts. The right-lateral strike-slip fault zone between C0002 and C0001 is drawn after *Martin et al.* [2010]. The far-field convergent vector between the Philippine Sea plate and Japan is marked with arrows in Figure 1a [*Seno et al.*, 1993].

ranges of stress magnitudes that can create the observed failures. Despite the lack of available parametric data, our analysis yields meaningful results that demonstrate a dynamic spatial variation of the stress state in this tectonically dynamic region.

2. Observation of Borehole Wall Failures and Stress Directions

[6] The drilling sites are located near the southern edge of the Nankai fore arc, southwest of the Kii Peninsula, Japan. In the first expedition of NanTroSEIZE, multiple boreholes were drilled and logged using the LWD technique. A rotary drill bit was immediately followed by a series of logging tools connected to the bottomhole assembly that measured a number of different geophysical data such as resistivity images, density, and sonic velocity, as well as drilling parameters such as borehole mud pressure during drilling. Drilling was conducted in riserless mode using drilling vessel *Chikyu*.

[7] In this paper, we present results from four boreholes (C0002, C0001, C0004 and C0006, from NW to SE), where the LWD resistivity logs capture images of borehole wall failures (Figure 2). Based on logged physical properties and seismic sections in this site, the boreholes were found to penetrate multiple geologic domains, which are divided by major and minor structural boundaries such as unconformities, boundaries between different thrust sheets, or the megasplay fault [*Tobin et al.*, 2009].

[8] Resistivity imaging logs provide a high-resolution picture of the borehole wall based on resistivity contrasts that allows for the direct observation of borehole breakouts, which look as broad, parallel conductive zones separated by 180° (as shown in the unwrapped images in Figure 2). Breakouts are electrically conductive, because the borehole fracturing and spalling associated with the breakout results in poor contact between the tool pads and the borehole wall, which in turn causes the tool to partially or fully measure the resistivity of the electrically conductive borehole fluid rather than the formation [*Tingay et al.*, 2008]. Because borehole breakouts in a vertical hole form at two diametrically opposed zones aligned with the least in situ horizontal principal stress direction where the local stress concentration is maximum [e.g., *Bell and Gough*, 1979; *Mastin*, 1984; *Haimson and Herrick*, 1985], they can be utilized as an important indicator of the direction of far-field horizontal stresses.

[9] Another feature of borehole wall failure is vertical drilling-induced tensile fractures (DITFs) at some depths in borehole C0001 (Figure 2b). In a vertical hole, DITFs tend to occur in the direction parallel to the maximum horizontal principal stress, when the local hoop stress there becomes tensional and its magnitude exceeds tensile strength of the rock [*Bell*, 1996; *Brudy and Zoback*, 1999]. Thus, the DITFs can be utilized as an indicator of the in situ stress orientation and possibly as a constraint of its magnitude as well.

[10] The borehole failure is a result of interplay between in situ stress, rock strength, and drilling parameters such as borehole pressure [*Zoback*, 2007]. Riserless drilling has no direct control over borehole pressure, which is normally intended to be hydrostatic seawater pressure. At significant depths (as shown in C0001 and C0002 in Figure 3), however, the borehole pressure often increased over the hydrostatic water pressure through surface pumping of drilling mud. For example, the annulus pressure (APRS) in C0002 increases approximately linearly at a rate slightly higher than hydrostatic, resulting in a value ~2 MPa higher than hydrostatic at the bottom hole. Although there were no noticeable drilling problems in this hole, the elevated borehole pressure over hydrostatic means that even in riserless drilling, the borehole pressure can be affected and controlled to some degree using surface pumping. Some general observations on the borehole wall failures in individual boreholes (from NW to SE) are as follows.

2.1. C0002

[11] At C0002, borehole breakouts are detected continuously below 200 mbsf (meters below seafloor) to the bottom of the hole (1401.5 mbsf). We picked the azimuths and widths of the breakouts and averaged them every 30 m depth interval to utilize them for stress tensor estimation. To evaluate the averages of the azimuth and width, we took the height of picked individual breakout zones as weighting factor. As shown in Figure 3, the pairs of BOs have nearly consistent azimuths throughout this vertical hole, with averages of 133 ± 14° and 310 ± 13°, indicating that the direction of the maximum horizontal principal stress (S_{Hmax}) at this site is overall NE-SW (41 ± 14°). There is a slight and gradual change in azimuth with depth from ~125° in the upper fore-arc basin to ~145° in the lower part of the prism. The S_{Hmax} orientation indicated by the breakouts at the lower prism is notably margin-parallel.

[12] The width of BOs varies with depth (see, e.g., changes in breakout width within logging unit II at 450 mbsf and at the boundary between logging units II and III at 850 mbsf). Especially noted is a sharp increase in BO width at the unconformity between the fore-arc basin and the old underlying accretionary prism penetrated by the borehole (boundary between logging unit III and IV in Figure 3a). The average width is notably larger in the lower section of the hole (70–100° in logging unit IV) than in the upper section (30–50° in logging unit II and III).

2.2. C0001

[13] Variation of borehole wall failure is more drastic in C0001 (Figures 2b and 3b). The BOs form almost continuously in logging unit I (slope sediments) and II (upper accretionary prism), and sporadically in logging unit III (lower accretionary prism). The breakout orientations are consistent throughout the hole, with averages of 63 ± 15° and 247 ± 16°. The average widths of breakouts vary in a range of 25–50° in logging unit I and II (notably

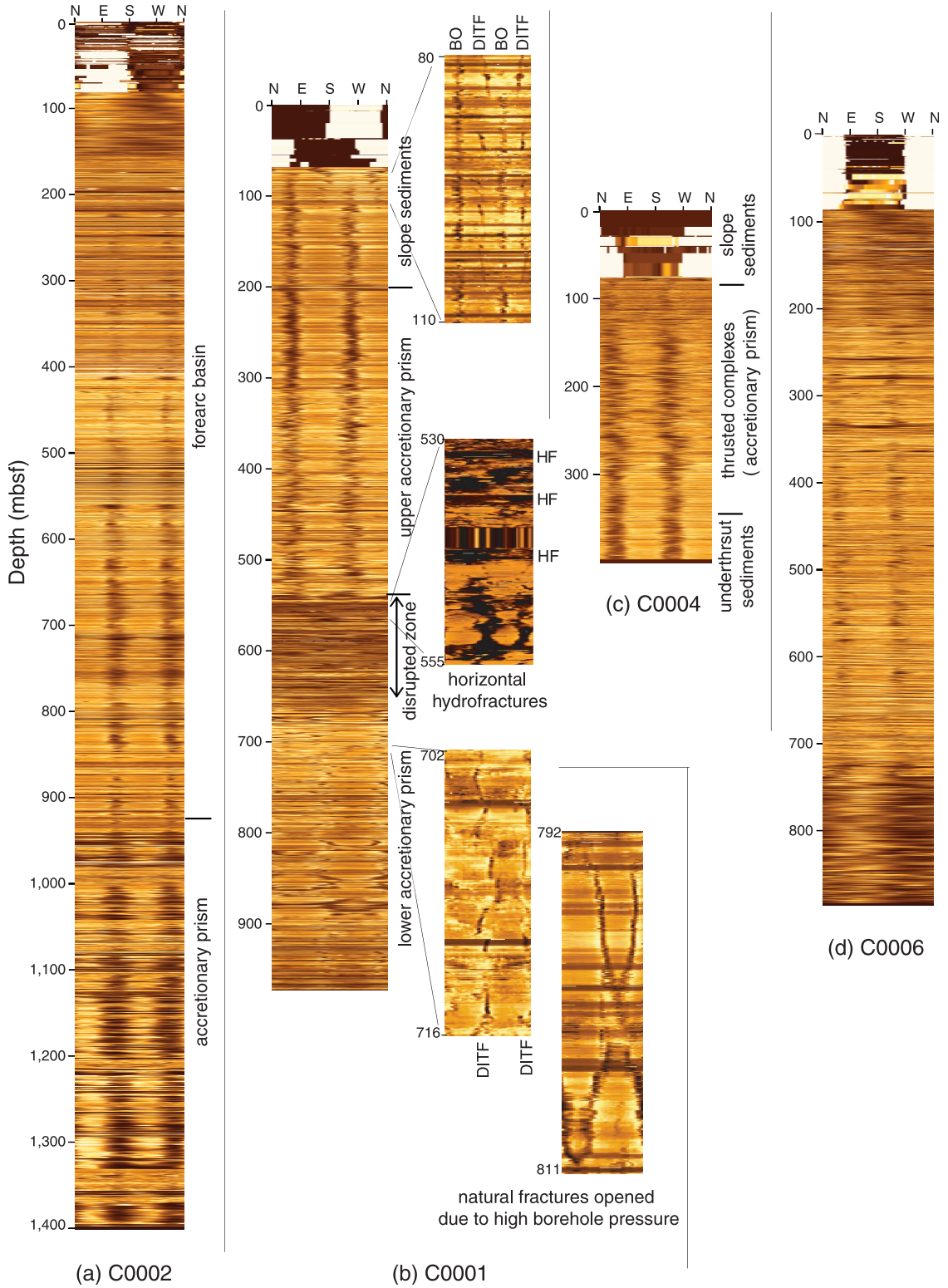

Figure 2. Unwrapped borehole resistivity images in (a) C0002, (b) C0001, (c) C0004, and (d) C0006, showing drilling-induced borehole wall failures. Borehole breakouts are manifested by a pair of vertical dark (electrically conductive) zones. Drilling-induced tensile fractures (DITFs) are common in shallow slope sediments and the lower accretionary prism. Some examples of DITFs are shown in close-up views.

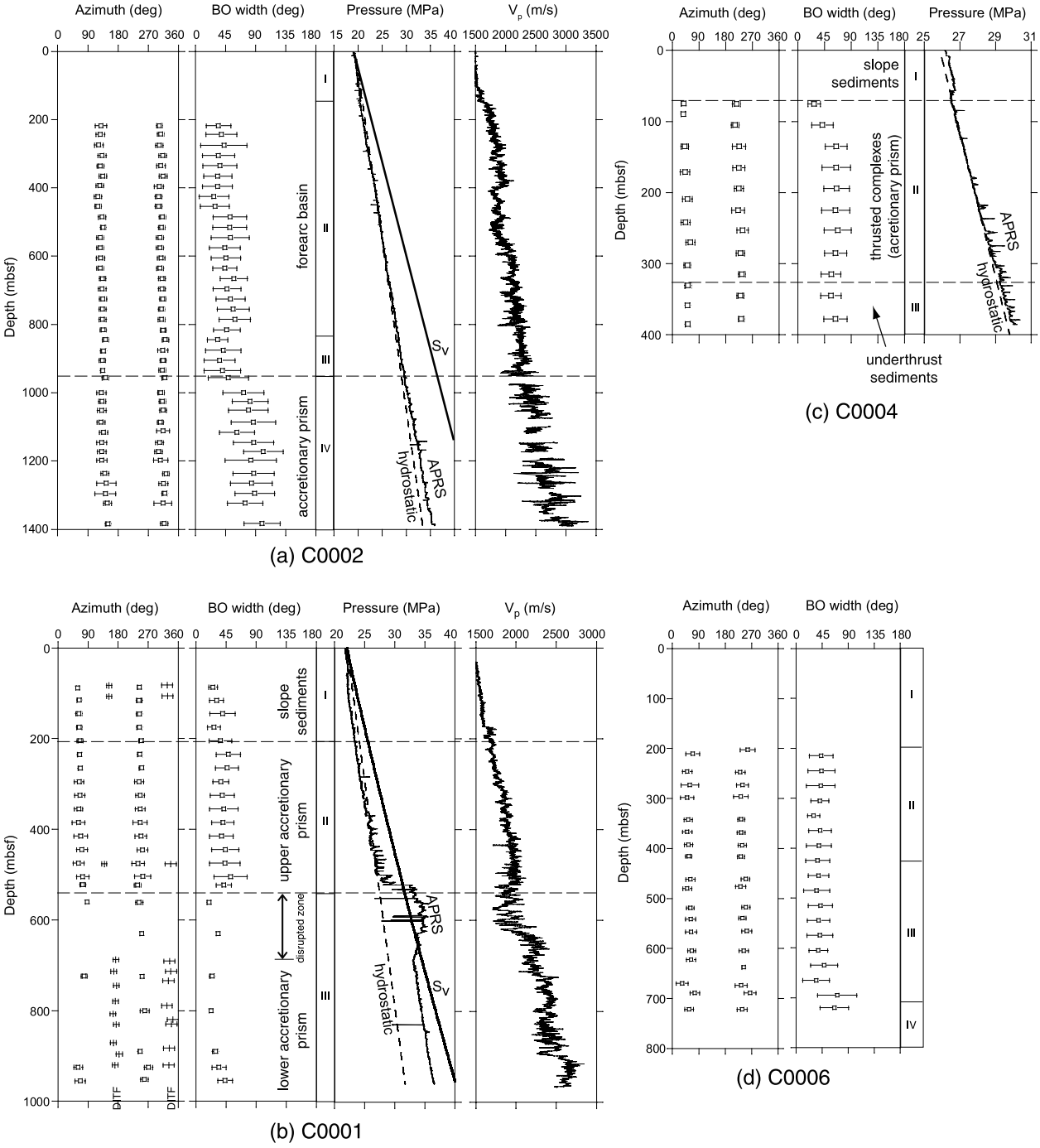

Figure 3. Orientations and widths of borehole breakouts (squares) and drilling-induced tensile fractures (vertical bars in Figure 3b) averaged at every 30 m depth interval in (a) C0002, (b) C0001, (c) C0004, and (d) C0006. Horizontal error bars indicate standard deviations in azimuth and breakout width. Juxtaposed are log-based units (marked as roman numerals), pressure profiles (annulus pressure (APRS), hydrostatic pressure, and vertical stress calculated from overburden (S_v)), and sonic velocity profile (V_p). No density in C0004 and drilling parameters in C0006 were measured.

at the boundary between logging units). In logging unit III, BOs are rare, and even for the limited number of breakout zones, their widths are significantly narrower than those in the upper units.

[14] Severe difficulties in drilling (increased surface torque and stick-slip on the drill pipe) were encountered below 520 mbsf. The surface pumping pressure was raised to clean the hole, which consequently

increased the annulus pressure to a value as high as that corresponding to an equivalent circulating density (ECD) of 1.3 g/cm^3. The annulus pressure in a depth interval between 520 and 660 mbsf was above the vertical stress (S_v) calculated from overburden density (Figure 3b), which caused significant formation damage and disruption probably associated with horizontal hydrofracturing. Although it is difficult to clearly distinguish the horizontal hydraulic fracturing from inherent horizontal features of the formations such as bedding planes in the borehole image, the overall dark color (low resistivity) in this interval compared to the rest of the hole indicates enhanced conductivity, which is attributed to flow-out through hydrofractures (see Figure 2b). Below ~690 mbsf, the pressure gradient stayed at near-hydrostatic, but the values themselves were maintained at ~5 MPa above hydrostatic water pressure. This fact indicates that the depth interval below ~690 mbsf was sealed somehow, for instance, due to a tight hole.

[15] In the top 110 m interval and below ~660 mbsf, numerous drilling-induced tensile fractures (DITFs) are observed (Figure 2b). The DITFs are subvertical (less than 3° of tilting) in this vertical hole, confirming that one of the principal stresses is also vertical (S_v). DITFs in C0001 are common in logging unit III, since the increased borehole pressure over the hydrostatic tends to induce local tensile hoop stresses at the borehole wall. It is also noted that several steeply inclined natural fractures open widely due to high borehole fluid pressure (see example at 792–811 mbsf in Figure 2b). Throughout the borehole, the azimuths of the DITFs are consistent, with averages of 168 ± 20° and 333 ± 10°. There is a minor asymmetry of ~15° in the average orientations of DITFs, which might be attributed to inhomogeneity of tensile strength over borehole perimeter due to preexisting fractures. The azimuths of BOs and DITFs are nearly perpendicular, consistently indicating the minimum and maximum horizontal principal stress directions. An immediate result from the BOs and DITFs is that the S_{Hmax} direction is NNW-SSE (156 ± 16°) at site C0001, which is nearly perpendicular to that at C0002.

2.3. C0004

[16] The logging units I, II and III, corresponding to the three structural domains (slope sediments, accretionary prism, and underthrust sediments, respectively) show different patterns of borehole breakouts (Figures 2c and 3c): no or weakly developed BOs in unit I, slightly variable BO orientation in unit II, and clear and consistent shape and orientation in unit III. The average breakout orientations are 47 ± 15° and 226 ± 20°, indicating that S_{Hmax} direction is NW-SE (136 ± 15°). The width of BOs is nearly constant with an average of 65° below ~130 mbsf in the thrust wedge, but it decreases slightly to 55° in the underthrust sediments.

2.4. C0006

[17] Borehole breakouts and associated wall failure occur in logging unit II, III and IV (Figures 2d and 3d). In units II and III, breakouts are developed with consistent orientations (60 ± 16°) and widths (40 ± 21°). In unit IV, breakouts appear to be enlarged in width and eventually take the form of an elongated borehole washout, which is confirmed by the four-directional sonic caliper logs [*Tobin et al.*, 2009]. Unfortunately, data for drilling parameters are not available in this hole (because of malfunction of some of the logging tools), and no detailed geomechanical analysis for these features is possible. Based on the breakouts with finite widths, the mean S_{Hmax} orientation is determined to be NW-SE (150 ± 16°), subparallel to that observed at C0001 and C0004.

3. Use of Borehole Wall Failures to Constrain Stress Magnitudes

3.1. Method Background

[18] We attempt to constrain in situ stress magnitudes in C0001 and C0002, where all necessary data are available. Vertical stress (S_v) is calculated from overburden (utilizing density logs). A normal method of stress magnitude estimation is as follows. For a given least horizontal principal stress (S_{hmin}), which is often measured through various borehole experiments (hydrofracturing tests and leak-off tests), a range of the S_{Hmax} value is estimated based on the borehole wall failures [e.g., *Brudy et al.*, 1997; *Haimson and Chang*, 2002]. Since no information on S_{hmin} values is available in riserless drilling here, we estimate both ranges of S_{hmin} and S_{Hmax} that could possibly result in the observed borehole wall failures.

[19] We first assume that the stress state is limited by Coulomb frictional sliding on optimally oriented faults [*Zoback*, 2007]. This means that if the ratio between the two extreme effective principal stresses goes beyond certain values defined by the coefficient of friction (μ) of nearby faults, sliding occurs along critically oriented faults, which consequently

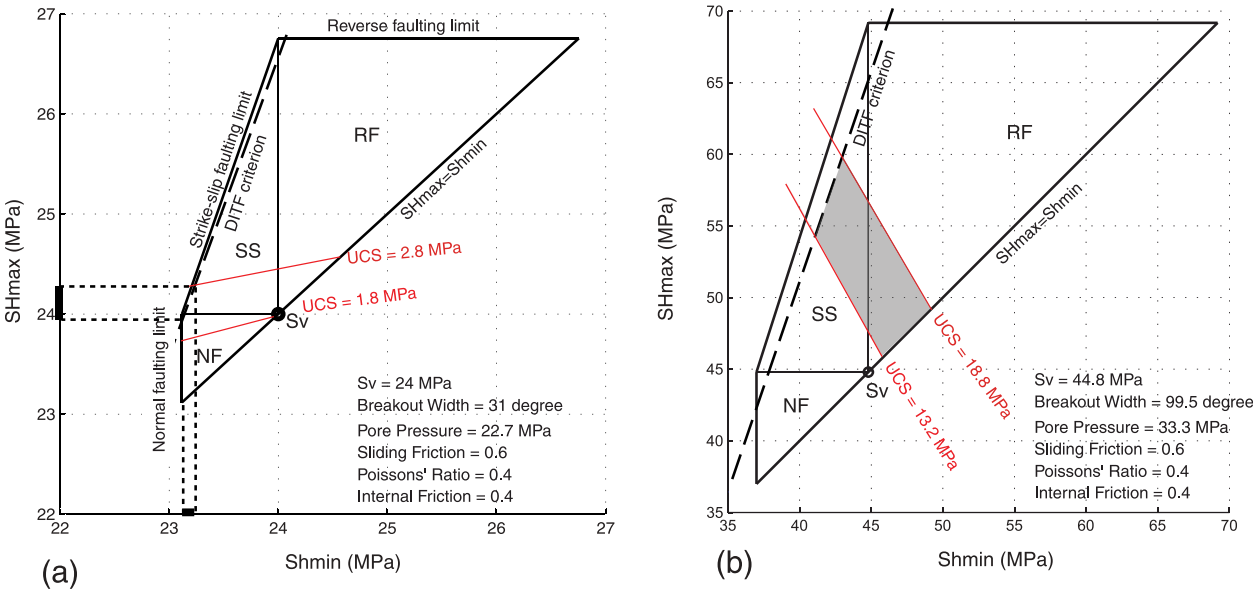

Figure 4. Two examples of stress polygon defined by Coulomb friction law with a friction coefficient of 0.6 and hydrostatic pore pressure, which encompass allowable S_{Hmax} and S_{hmin} magnitudes for given S_v. The drilling-induced tensile fracture (DITF) criterion defines a threshold, above which local tensile hoop stress is induced. The uniaxial compressive strength (UCS) red lines indicate the traces of S_{Hmax} magnitudes (as a function of S_{hmin}) required to cause breakouts with a certain width for the UCS values labeled. (a) The example at a depth of 110 m in C0001, where both BOs and DITFs are observed, shows that S_{Hmax} and S_{hmin} magnitudes are in the ranges marked by dotted lines. (b) At 1382 m in C0002, where only BOs are observed, the constrained S_{Hmax} and S_{hmin} range should lie in the shaded area.

limits the stress state. More explicitly, the condition for frictional limit can be expressed:

$$\frac{\sigma_1}{\sigma_3} = \frac{S_1 - P_p}{S_3 - P_p} = \left(\sqrt{\mu^2 + 1} + \mu\right)^2 \quad (1)$$

where σ_1 and σ_3 are effective maximum and minimum principal stresses; S_1 and S_3 are the maximum and minimum in situ principal stresses, respectively; P_p is pore pressure. With S_1 and S_3 being one of S_v, S_{Hmax} and S_{hmin}, depending on the stress regime, equation (1) can be plotted as three lines in the S_{Hmax} versus S_{hmin} domain, defining the stress polygon (Figure 4). For a given depth, the size of stress polygon depends on μ and P_p: either increasing μ or decreasing P_p makes the size of polygon larger. Under stress conditions outside the stress polygon, the rock would be at failure in its natural state. The interior of the stress polygon defines allowable values for horizontal principal stresses for conditions favoring normal, strike-slip, or reverse faulting. Thus, the stress polygon encompasses the possible states of stress at a given depth.

[20] Further constraints of stress magnitude can be made using the presence of DITFs and widths of BOs combined with rock strength information [e.g., *Zoback*, 2007; *Shen*, 2008]. The drilling-induced borehole wall failures are a signature of the local stress conditions at the borehole wall, which is derived from the far-field in situ stress and borehole conditions. With the assumption of plane strain condition at the borehole wall (no strain in vertical direction), the three effective principal stresses acting on the initially circular borehole wall, $\sigma_{\theta\theta}$ (hoop stress), σ_{zz} (vertical stress), and σ_{rr} (radial stress), are expressed as [*Jaeger et al.*, 2007]:

$$\begin{aligned} \sigma_{\theta\theta} &= S_{\mathrm{Hmax}} + S_{\mathrm{hmin}} + 2(S_{\mathrm{Hmax}} - S_{\mathrm{hmin}})\cos 2\theta - P_p - APRS \\ \sigma_{zz} &= S_v + 2\nu(S_{\mathrm{Hmax}} - S_{\mathrm{hmin}})\cos 2\theta - P_p \\ \sigma_{rr} &= APRS - P_p \end{aligned} \quad (2)$$

where θ is the azimuth angle from the S_{hmin} direction; APRS is annulus pressure (or borehole pressure applied by mud weight); ν is Poisson's ratio. We assume hydrostatic pore pressure based on recent MDT measurements at a nearby site [*Saffer et al.*, 2009]. It is also noted that pore pressure monitoring instruments installed at the Nankai frontal thrust at several depths down to ~878 mbsf recorded pressure levels slightly elevated (by less than 0.2 MPa) above hydrostatic [*Sawyer et al.*, 2008], which is definitely within the uncertainty range and does not affect our results significantly. More analysis on pore pressure and its sensitivity on

in situ stress estimation are discussed later. The three effective principal stresses given in equation (2) are normally unequal ($\sigma_{\theta\theta} \neq \sigma_{zz} \neq \sigma_{rr}$); that is, borehole wall rock is subjected to true triaxial stresses.

[21] DITFs occur when the hoop stress $\sigma_{\theta\theta}$ at the borehole wall exceeds tensile strength of the formation. Throughout our analysis, we assume that the tensile strength of the rock is negligible in these weak sedimentary formations. This means that DITFs occur essentially when the local hoop stress at the borehole wall is tensile (i.e., $\sigma_{\theta\theta} < 0$). In Figure 4, the DITF line defines the criterion for creation of DITF, above which local hoop stress can be tensile. The occurrence of DITFs in the upper 110 mbsf of C0001 indicates that the state of stress should lie somewhere above the DITF line in the example shown in Figure 4a, but within the stress polygon drawn with $\mu = 0.6$. The observation of DITFs indicates that the coefficient of friction should be at least 0.6 or higher in order to allow a possible stress range that can induce tensile hoop stresses at the borehole wall. Since weak sediments tend to have low resistance to shear stress [*Kopf and Brown*, 2003], we assume the minimum value, $\mu = 0.6$, for the static friction coefficient.

[22] The widths of BOs have been utilized for stress magnitude estimation when rock strength information is available. The premise behind this analysis is that the broken-out zone is where the local stress condition exceeds rock strength, and the intact zone is where the former does not exceed the latter. Thus the intersection between the initial circular borehole cross section and borehole breakout is the point where the stress state is equal to rock strength [e.g., *Haimson and Herrick*, 1986; *Barton et al.*, 1988; *Vernik and Zoback*, 1992]. Thus, if rock strength information is available, it is possible to further constrain stress conditions that cause the observed widths of borehole breakout. In section 3.2, we describe how we derive rock strength.

3.2. Estimation of Rock Compressive Strength

[23] The stress conditions at rock failure are described by strength criteria, which are expressed in terms of the maximum principal stress at failure as a function of the other two principal stresses [*Scholz*, 1990]. It is important to emphasize that rock strength is affected not only by the least principal stresses, but also by the intermediate principal stresses based on numerous previous studies (see reviews by *Chang and Haimson* [2000], *Colmenares and Zoback* [2002], and *Benz and Schwab* [2008]). Because the stress condition at the borehole wall is true triaxial, a precise prediction of rock strength requires the utilization of true triaxial strength criteria, in which all the three principal stresses are incorporated. Various such failure criteria of rock have been proposed, and their characteristic features have extensively been studied [*Colmenares and Zoback*, 2002; *Benz and Schwab*, 2008]. We use the modified Wiebols and Cook criterion [*Zhou*, 1994] because it was shown to be quite reliable when compared to real rock strength data under generalized stress conditions, which is especially important for rock failure at the borehole wall [*Colmenares and Zoback*, 2002]. The modified Wiebols and Cook criterion has the form:

$$J_2^{1/2} - A - BJ_1 - CJ_1^2 = 0 \tag{3}$$

where

$$J_1 = (\sigma_1 + \sigma_2 + \sigma_3)/3,$$

$$J_2 = \left((\sigma_1 - \sigma_2)^2 + (\sigma_2 - \sigma_3)^2 + (\sigma_3 - \sigma_1)^2\right)/6,$$

$$C = \frac{\sqrt{27}}{(2C_1 + (q-1)\sigma_3 - UCS)} \cdot \left(\frac{C_1 + (q-1)\sigma_3 - UCS}{2C_1 + (2q+1)\sigma_3 - UCS} - \frac{q-1}{q+2}\right)$$

$$\text{with} \quad C_1 = (1 + 0.6\mu_i)UCS \text{ and } q = \left(\sqrt{\mu_i^2 + 1} + \mu_i\right)^2,$$

$$B = \frac{\sqrt{3}(q-1)}{q+2} - \frac{C}{3}(2UCS + (q+2)\sigma_3), \text{ and}$$

$$A = \frac{UCS}{\sqrt{3}} - \frac{UCS}{3}B - \left(\frac{UCS}{3}\right)^2 C.$$

Although the modified Wiebols-Cook criterion has a somewhat complicated form, it is parameterized only with the two material properties, uniaxial compressive strength (UCS) and internal friction coefficient (μ_i) [*Jaeger et al.*, 2007], which can be determined from conventional triaxial tests.

[24] A few conventional triaxial compression tests were conducted on core samples extracted from the boreholes from this transect to measure rock strength and deformability, including UCS and μ_i. All samples (even the extremely high porosity sediments) failed in brittle mode with a major inclined shear fracture, which reaffirms the possibility of breakout formation in shallow sediments. Table 1 lists physical/mechanical properties derived from these tests on intact rock cores (those from C0001 and C0002 kindly provided by CDEX). Given the limited rock strength data, we

Table 1. Rock Mechanical Properties of Nankai Cores

Borehole	Core Depth (mbsf)	UCS (MPa)	Internal Friction Coefficient	Poisson's Ratio	V_p (m/s)
C0001[a]	334	3.2	0.53	0.34	1843
C0002[a]	763	7.26	0.46	0.32	2116
	901	7.46	0.43	0.28	2128
	1021	4.12	0.28	0.31	1929
C0006	476	5.97	0.32	0.43	1854
C0007	393	5.33	0.54	0.42	1726

[a]Rock mechanics data in cores from C0001 and C0002 were provided by CDEX.

estimate strength properties indirectly based on empirical equations that relate rock strength with sonic velocity, V_p. The basis for these relationships is that many of the same factors that affect rock strength also affect velocity [*Chang et al.*, 2006]. Such an approach is well utilized in the petroleum industry when no cores for rock testing are available, and it is practical since boreholes penetrate different formations with continuously varying mechanical properties. Figure 5 shows several UCS-V_p relations calibrated through laboratory experiments on high-porosity shaley sediments in different basins worldwide [*Lal*, 1999; *Horsrud*, 2001; *Chang et al.*, 2006]. Also plotted are strength data from the Nankai trough cores (given in Table 1) and other data collected from the literature [*Lama and Vutukuri*, 1978; *Carmichael*, 1982; *Horsrud*, 2001]. Although predicted UCS values for a given velocity differ somewhat depending on different relationships, there is a general similarity in their overall increasing trend of UCS with increasing velocity. The range of UCS as a function of velocity, for both the empirical relations and the majority of data set, is quite well constrained within ±4 MPa in the velocity range that covers the logged V_p ranges of the boreholes. Based on the UCS data from C0001 and C0002 cores, we take the empirical relationships A and C as the lower and upper bounds of strength, respectively.

[25] For the internal friction coefficient (μ_i), we use the average value of 0.4. It is noteworthy that the impact of internal friction coefficient on strength criterion has much less significance than that of UCS [*Chang et al.*, 2006]. Also if borehole pressure is similar to pore pressure (i.e., $\sigma_r \sim 0$) as in most cases of the present study, the significance of internal friction coefficient is minor.

3.3. Constraining Stress Magnitudes

[26] While S_{hmin} magnitudes are relatively readily estimated using various borehole techniques such as leak-off tests and hydraulic fracturing tests, those for S_{Hmax} are known to be difficult to estimate because no known clear and direct determination methods are available. Obviously when both S_{hmin} and S_{Hmax} are unknown as in our case, the constrained stress magnitudes are subject to reliability issue. However, accepting that the observed borehole breakouts are those soon after drilling and has not been altered by any other factors affecting their widths and that their formation is due to brittle failure of borehole wall rock as a response of the localized stress around borehole as manifested by previous laboratory experiments, we believe that the constrained ranges of stress that will be shown

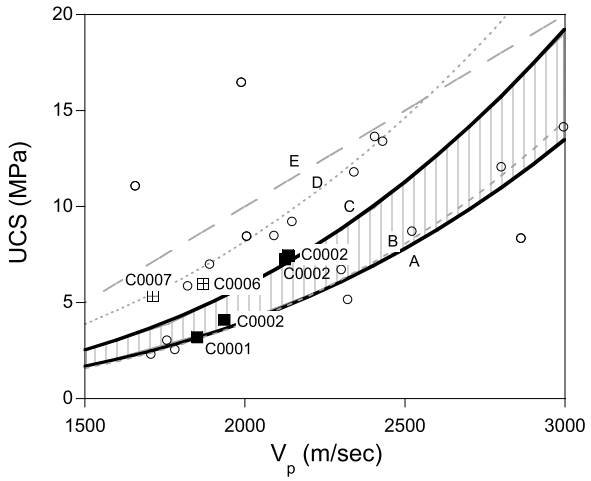

Figure 5. Empirical correlations that relate uniaxial compressive strength (UCS) with sonic velocity (V_p) that are calibrated for poorly consolidated shaley rocks: A, Gulf of Mexico shale [*Chang et al.*, 2006]; B, Gulf of Mexico shale [*Chang et al.*, 2006]; C, North Sea shale [*Horsrud*, 2001]; D, compiled shale data worldwide [*Chang et al.*, 2006]; E, North Sea shale [*Lal*, 1999]. Experimental data on cores from C0001, C0002, C0006, and C0007 (input site close to C0006 [*Tobin et al.*, 2009]), as well as data from literature (circle) [*Lama and Vutukuri*, 1978; *Carmichael*, 1982; *Horsrud*, 2001], are overlapped. In this study, relationships A and C are taken as the lower and upper bounds, respectively, of UCS as a function of V_p.

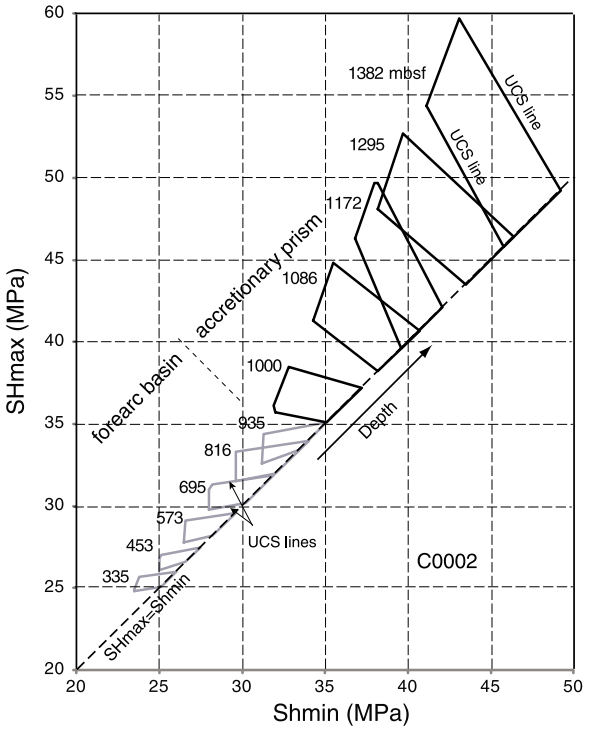

Figure 6. Constrained S_{Hmax} and S_{hmin} magnitudes in C0002 based on the observed borehole breakouts at different depths.

below give a good guideline to the in situ stress magnitudes.

[27] If we assume that the local stress state at the margin of breakouts (at θ = BO width/2) is equal to that of rock failure, it is possible to derive an equation by combining equations (2) and (3), which is depicted in the stress polygon by a stress range bounded by UCS lines in the Figure 4. Thus, for a depth of 110 m in C0001, where we observe both BOs and DITFs, the possible S_{Hmax} and S_{hmin} magnitudes are extremely well constrained within the range enclosed by the polygon, DITF criterion, and UCS lines (Figure 4a). As another example in Figure 4b, at a depth of 1382 m in C0002, where we observed large BOs without DITFs, the possible ranges of S_{Hmax} and S_{hmin} are within the shaded area in order to create the borehole failures we observed. The ranges are relatively wide, but it is clear that the stress regime there is in favor of either strike-slip, or reverse faulting.

[28] Using the same methods, stress magnitudes are estimated in C0001 and C0002. Figure 6 shows the possible ranges of S_{Hmax} and S_{hmin} magnitudes at several depths in C0002. It is obvious that the magnitudes of S_{Hmax} and S_{hmin} increase with depth. The general shape of the stress ranges differs between the fore-arc basin and the accretionary prism. In the fore-arc basin, the UCS lines bounding the upper and lower polygon are subhorizontal, indicating that the range of S_{Hmax} does not change significantly for different S_{hmin} values. On the contrary, the UCS lines for the accretionary prism stress are steeply inclined, indicating that the S_{Hmax} range should differ significantly depending on S_{hmin} values. For example, at a depth of 1382 mbsf, if actual S_{hmin} is close to its lower limit (say, 41 MPa), the possible S_{Hmax} magnitudes should be quite high (53–57 MPa), whereas if S_{hmin} is high (say, 47 MPa), the possible S_{Hmax} values are low (48–51 MPa). This emphasizes the importance of reliable measurements in S_{hmin} value in the accretionary prism.

[29] Figure 7 summarizes the constrained in situ stress profile at all the depths we analyzed in C0002 and C0001. In the fore-arc basin sediments between 400 mbsf and the unconformity in C0002, the ranges of the two horizontal principal stresses lie below S_v, indicating a normal faulting stress regime. Above 400 mbsf, however, the stress regime is not well distinguished, because the differential stresses between principal stresses are extremely small (meaning small sizes of stress polygon). From just below the unconformity, the ranges of the two horizontal principal stresses appear to increase at higher rates with depth than the S_v gradient. While a large portion of the possible S_{hmin} lies below S_v, the S_{Hmax} range is predominantly higher than S_v, indicating that the stress state in the accretionary prism is likely a strike-slip faulting stress regime. Still, there is some ambiguity in this stress profile, since the stress regime in the accretionary prism can strictly be any of normal, strike-slip or reverse faulting, depending on S_{Hmax} and S_{hmin} magnitudes. However, as we showed above in Figure 6, the S_{Hmax} and S_{hmin} are not arbitrarily correlated, but defined by a range enclosed with a characteristic shape of polygon. In other words, both S_{Hmax} and S_{hmin} cannot be at their lower bounds simultaneously. More detailed discussion about stress regime will be covered later.

[30] For C0001 (Figure 7b), in the upper part of the borehole (<500 mbsf), the ranges of S_{Hmax} and S_{hmin} are slightly lower than, or quite similar to S_v, indicating that the stress regime is predominantly in favor of normal faulting. In the lower accretionary prism, it is clearly seen that S_{Hmax} is higher than S_v, while S_{hmin} in most depths remains lower than S_v, indicating predominantly a strike-slip faulting stress regime, or possibly a reverse faulting stress regime when $S_{hmin} > S_v$.

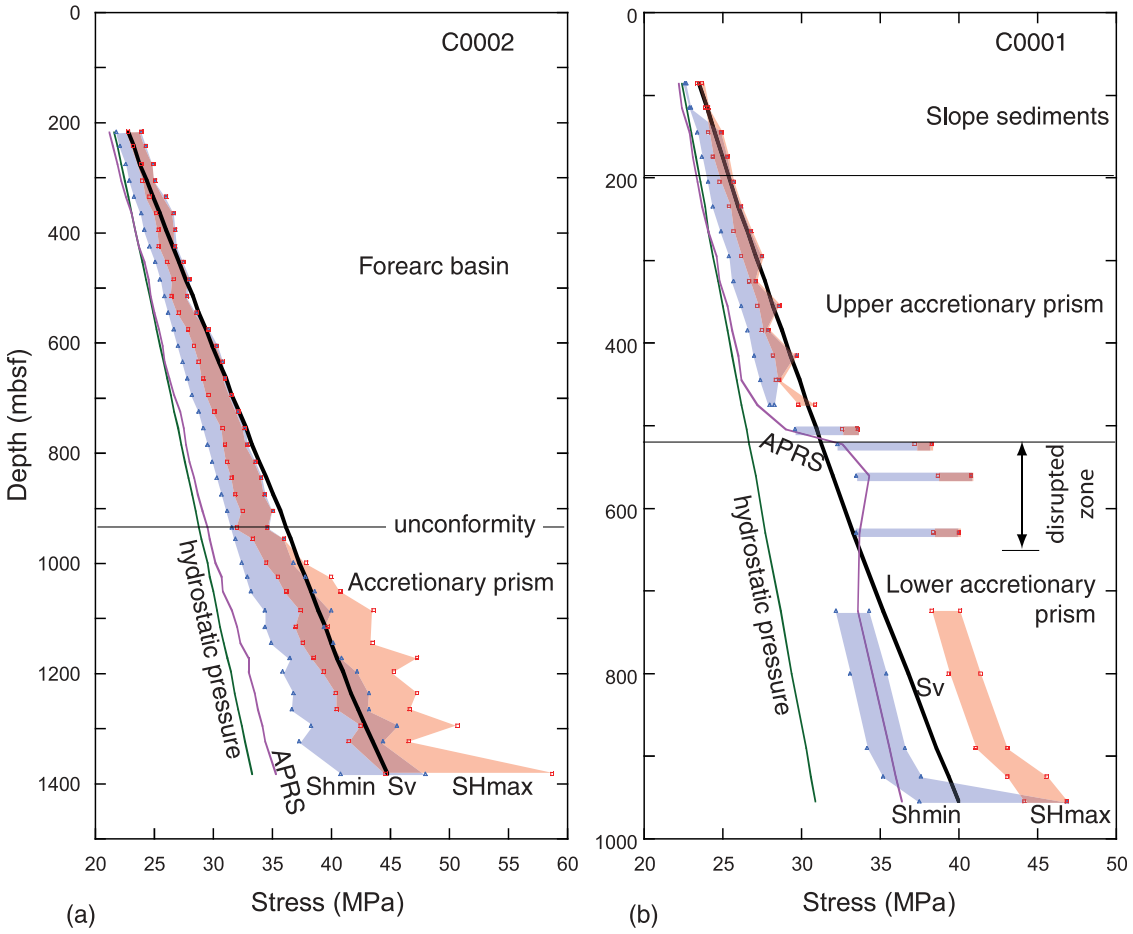

Figure 7. The constrained in situ stress profile with depth in (a) C0002 and (b) C0001. For stress estimation, pore pressure is assumed hydrostatic throughout. In the shallow depths (fore-arc basin in C0002 and slope sediments and upper accretionary prism in C0001), the two horizontal principal stresses (S_{Hmax} and S_{hmin}) are generally lower than S_v that is calculated from overburden, suggesting a normal faulting stress regime. At the greater depths, S_{Hmax} appears to be larger than S_v, suggesting that the stress regime there is in favor of most likely strike-slip faulting. See text for details.

[31] In the lower accretionary prism, the resistivity image shows that numerous steeply dipping natural fractures striking to subparallel to S_{Hmax} direction exhibit wide apertures (see open tensile fractures in Figure 2b, for example). These fractures are interpreted to be natural fractures since some of them are cut by other faults [*Tobin et al.*, 2009], and opened by the excess borehole pressure that was raised significantly higher than hydrostatic. The wide apertures of these fractures may be an indicator of hydraulic fracturing process through these fractures, which implies that the borehole pressure is overcoming the least horizontal principal stress. This provides a further constraint suggesting that S_{hmin} may be lower than the borehole pressure (APRS), close to the lower bound of the estimated S_{hmin} range in Figure 7b.

[32] Our results overall suggest a variation of stress regime in different geologic domains. To visualize the change in stress regimes, Figure 8 shows the ranges of S_{Hmax} and S_{hmin} normalized by S_v at different depths. In the fore-arc basin at C0002, the areas enclosed by the normalized polygons lie mainly in the normal faulting stress regime where both S_{Hmax}/S_v and S_{hmin}/S_v are generally smaller than unity. In the accretionary prism, the S_{Hmax}/S_v ratio increases markedly above unity, resulting in most likely a strike-slip or a reverse faulting stress regime depending on S_{hmin} value.

[33] In the upper part of C0001 (slope sediment and upper accretionary prism), the ratios of S_{Hmax}/S_v and S_{hmin}/S_v are generally less than unity, confirming that the stress state is in favor of normal faulting. In the disrupted zone where the borehole pressure increased over overburden, both horizon-

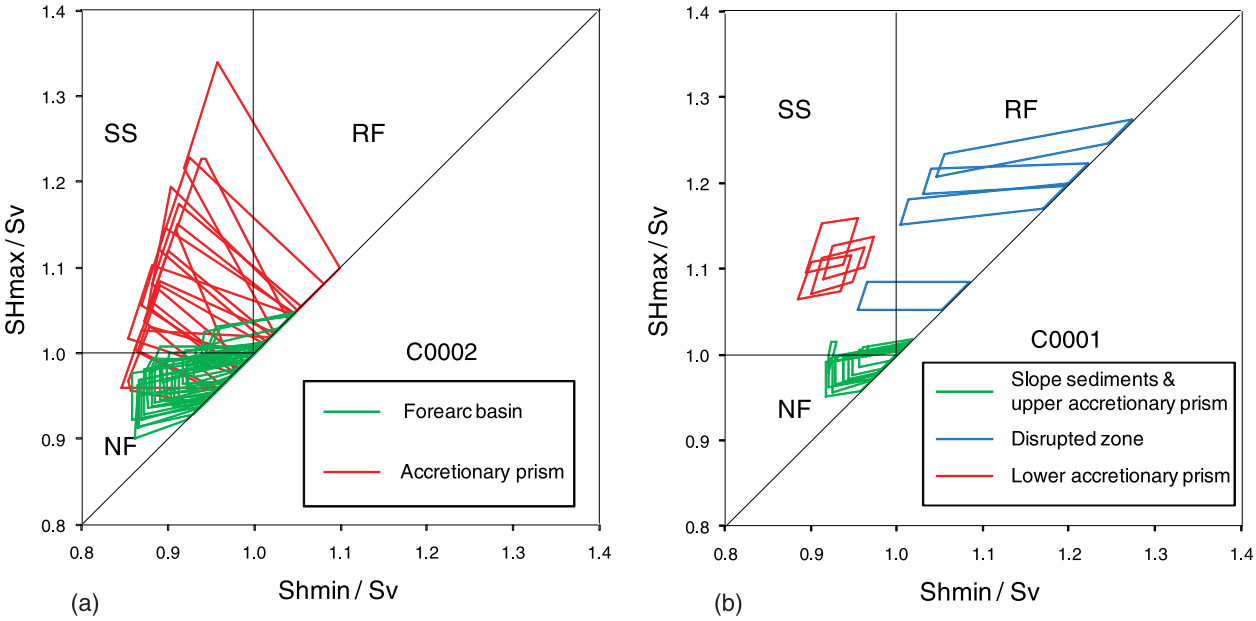

Figure 8. Constrained S_{Hmax} and S_{hmin} magnitudes normalized with S_v in (a) C0002 and (b) C0001, showing the variation of stress regimes in different geological domains. The stress regime varies in different structural domains.

tal stresses increase markedly above S_v, leading to a reverse faulting stress regime. In the lower accretionary prism domain, the S_{hmin}/S_v ratio predominantly decreases below unity, while the S_{Hmax}/S_v ratio remains larger than unity, suggesting a strike-slip faulting stress regime.

4. Discussion

[34] Overall, the shallow portion of the sites is characterized by a normal faulting stress regime, in which sedimentation-driven overburden is the major component of the stress tensor. This is in agreement with peak stress indicators from anelastic strain recovery in cores extracted from the same sites (C0001, C0002 and C0006) [*Byrne et al.*, 2009]. In the deeper accretionary prism, within the depths we investigated, the S_{Hmax} appears to be the maximum principal stress in both C0001 and C0002, indicating a likely strike-slip faulting stress regime. However, the orientation of the S_{Hmax} is nearly perpendicular at these two sites, suggesting that the major tectonic forces acting may be different in these sites, although the distance between them is only about 10 km.

[35] One of possible reasons responsible for the margin-parallel S_{Hmax} in the fore arc is a gravitation-driven, margin-normal extension, as manifested by the occurrence of active normal faults that strike to subparallel to the margin [*Tobin et al.*, 2009]. *Willett* [1999] discussed several different mechanisms that may be responsible for such an extension near the top of a critically tapered Coulomb wedge. Thus, it is expected that the margin-normal tectonic stress originated from pushing of the Philippine Sea plate would not propagate uniformly across the wedge. To examine this from our results, we compare the margin-normal stress components in C0001 and C0002. The S_{Hmax} directions at C0001, C0004 and C0006 sites are consistent with one another and subparallel (slightly oblique) to the subduction direction of the Philippine Sea plate, while at C0002, S_{hmin} direction is subparallel to these regional maximum compression. In Figure 9, the S_{Hmax} magnitudes in C0001 and the S_{hmin} in C0002 are overlaid as a function of depth below sea surface; thus, depths are leveled equally. The difference in water depth between these two sites is 261 m. While these two stress components at shallow depths above 2.7 km below sea surface are nearly comparable, there is a clear distinction (less compressive in C0002 than in C0001) between them at greater depths. This direct comparison may appear too simplistic because the stress state at a location can originate also from coupling between various factors such as gravity, pore pressure, and even the interaction between stress components. However, the stress difference in the two adjacent sites suggests that the in situ stress states in the accretionary

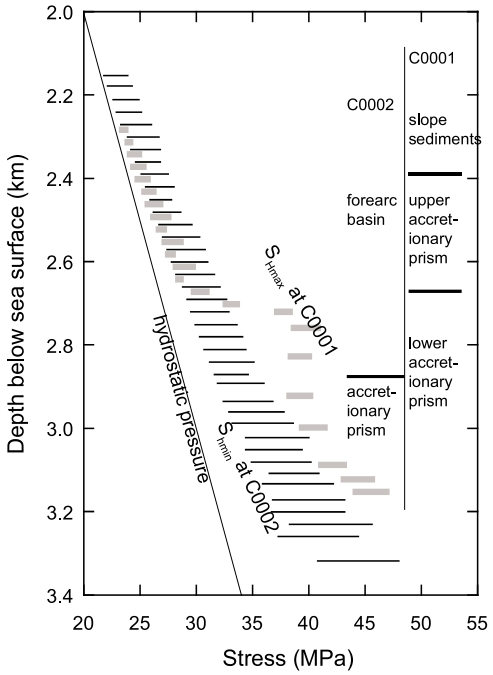

Figure 9. Comparison of the margin-perpendicular horizontal stress components between C0002 (S_{hmin}) and C0001 (S_{Hmax}), showing a discrepancy in stress magnitudes in the accretionary prism between the two sites. This suggests that tectonic stress field is not uniform between these two closely located sites.

wedge can be described not only by tectonic stress transfer, but also by some additional factors that affect stress states locally, as demonstrated by *Willett* [1999].

[36] It is interesting to note that the stress direction variation between the fore-arc and the outer arc domains remarkably resembles that seen in the delta-deepwater fold-thrust belt systems. *Tingay et al.* [2009] and *King et al.* [2010] showed that the maximum horizontal stress direction in a Tertiary delta, offshore northwestern Borneo, rotates from margin-parallel in the outer shelf (corresponding to fore arc here) to margin-normal in the inner shelf (delta toe). They also interpreted the margin-parallel S_{Hmax} in the outer shelf in terms of gravity-driven extension. In fact, *Bilotti and Shaw* [2005] showed that accretionary prisms as the critical taper wedge have a range of analogies with delta-deepwater fold-thrust belt systems based on their similarity in geometry. A major difference is an extremely low taper angle (sum of the bathymetric slope and dip of the basal detachment ~2°) in the delta system, implying an extremely weak basal detachment, compared to that of the accretionary wedge. This major difference may cause different strengths of plate coupling in the two systems, from which we can infer that their stress states may not be fully analogous at their whole scale. In fact, a recent observation on borehole stress indicators in a more landward Nankai fore-arc basin showed a margin-normal S_{Hmax} again [*Lin et al.*, 2010], which may be an indicator of higher plate coupling in the accretionary wedge than in the delta systems.

[37] Regarding the stress variation at smaller scale, factors that affect stress tensors could possibly include a deformation- (or mostly bending-) associated stress perturbation constrained within individual geologic units. Examples are either a localized bending within the anticlinal thrust sheets [*Cai et al.*, 1995] as in C0001, or a much larger scale plate bending associated with subducting slab that causes a stress localization depending on characteristic geometry and motion pattern of the slab [*Xu and Kono*, 2002; *Zhao et al.*, 2003]. In principle, these factors are related to inhomogeneous deformation that consequently induces local perturbation of in situ stress.

[38] Another interpretation on the stress variation is also possible from a geomechanics point view, considering the role of major discontinuities, which divide different structural domains and tend to diminish uniform stress propagation by sliding. One example is the trench-parallel depression in the seafloor between C0001 and C0002 sites, which is interpreted as an out-of-plane strike-slip fault zone from 3-D seismic image analysis [*Martin et al.*, 2010] (see Figure 1). It was suggested that there is a significant tectonic decoupling in the form of strain partitioning across the strike-slip fault zone. Such localized processes across the major boundaries are a possible source of the segmented stress regimes.

[39] The last issue we would like to discuss is pore pressure condition in the accretionary prism at depth this study covered. In our stress tensor estimation based on the borehole wall images, we assumed a hydrostatic pore pressure. However, pore pressure can often be higher than hydrostatic, particularly in the accretionary prism [*Mouchet and Mitchell*, 1989]. A rule of thumb is that the pore pressure cannot exceed annulus pressure for balanced and successful drilling, which otherwise would cause a number of severe drilling problems such as influx into boreholes, well kick, and stuck pipe. It is also obvious that the pore pressure in its natural state should not exceed any in situ stress components. Such a consideration may raise a doubt about the assumption of hydrostatic pore

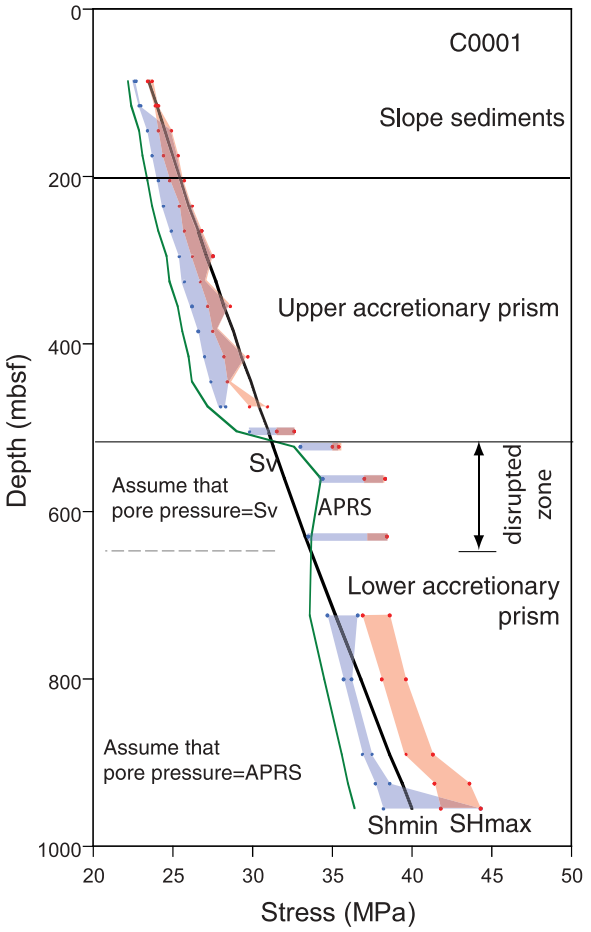

Figure 10. In situ stress profile with depth in C0001, where pore pressure may be higher than hydrostatic. In this analysis, pore pressure is assumed to be equal to either annulus pressure (APRS) or vertical stress (S_v), whichever is lower, which is thought of as the upper limit of possible pore pressure condition. The differences between the principal stresses are narrower than those when hydrostatic pore pressure is assumed in Figure 7b; however, the stress state in the lower accretionary prism is still predominated by a strike-slip faulting stress regime.

pressure in the accretionary prism blocks at C0001, where borehole annulus pressure was significantly higher than hydrostatic. In the lower accretionary prism at C0001, the possible upper bound of pore pressure could go up to value of either annulus pressure or lithostatic stress (S_v), whichever is lower. As we mentioned earlier, however, the widely open natural fractures in the lower accretionary prism, which are mostly aligned with perpendicular to the S_{hmin} direction (Figure 2b), suggest that the annulus pressure is likely to be higher than the S_{hmin} that in turn should be higher than pore pressure. Thus, the pore pressure is presumably quite lower than the borehole pressure.

[40] Just for sensitivity analysis, we used the extreme case of pore pressure that is equal to APRS or S_v, whichever is lower, to check whether the variation of stress regime in different structural domains is still valid in C0001. The assumed high pore pressure in the lower accretionary prism at C0001 site corresponds to the values of the pore pressure ratio (λ^*) of 0.57–1, where the pore pressure ratio is defined as

$$\lambda^* = (\text{pore pressure} - \text{hydrostatic pressure}) / (S_v - \text{hydrostatic pressure}). \quad (4)$$

The result of constrained in situ stress tensors with high overpressure assumed is plotted in Figure 10. When a larger pore pressure is used, the stress polygon drawn with equation (1) shrinks in size, which tends to reduce the difference between stress components. Thus, the differences between the three principal stresses are narrowed significantly compared to those when hydrostatic pore pressure is assumed (Figure 7b). Nonetheless, the general pattern of stress regime variation remains the same. That is, the lower accretionary prism is characterized by a strike-slip faulting stress regime.

5. Conclusions

[41] There is some degree of uncertainty (or wide ranges) in the constrained stress magnitudes, mainly due to insufficient data such as well constrained rock strength and some measured S_{hmin} values. However, the use of borehole wall failures provides detailed information on stress states in different locations and depths penetrated by the boreholes in the Nankai margin. Our attempt to constrain in situ stress orientations and magnitudes reveals that the in situ stress states and their regime vary between different geologic domains separated by the major and minor structural boundaries across and with depth in the Nankai fore arc. A normal faulting stress regime dominates in the shallow portion of the sites (shallow accretionary prism in C0001, fore-arc basin and slope sediments), in which sedimentation-driven overburden is the major component of stress tensor. In deeper domains (accretionary prism), the maximum horizontal principal stresses are the major component of the stress tensor, but approximately perpendicular between C0002 and C0001. In the accretionary prism, for the depth investigated, the stress state is most likely in favor of strike-slip

faulting. A comparison of the margin-perpendicular stress components between the two adjacent sites (C0002 and C0001) suggests that the stress state is not only driven by tectonic stress transfer, but also by additional factors presumably associated with localized deformation in different geological domains (such as gravitation-driven extension in the fore arc, and bending and thrusting in individual units).

Acknowledgments

[42] The data used herein were provided by the IODP. We thank CDEX for sharing the rock strength data. We also gratefully acknowledge the support provided by the D/V *Chikyu* drilling crew, logging staff, and laboratory technicians. The quality of paper was greatly enhanced by the constructive reviews from Mark Tingay and an anonymous reviewer. This research was supported by the R&D project "Integrated Ocean Drilling Program" of the Korea Institute of Geoscience and Mineral Resources (KIGAM) funded by the Ministry of Land, Transport and Maritime Affairs of Korea.

References

Barton, C. A., M. D. Zoback, and K. L. Burns (1988), In-situ stress orientation and magnitude at the Fenton geothermal site, New Mexico, determined from wellbore breakouts, *Geophys. Res. Lett.*, *15*, 467–470, doi:10.1029/GL015i005p00467.

Bell, J. S. (1996), In situ stresses in sedimentary rocks (part 1), Measurement techniques, *Geosci. Can.*, *23*, 85–100.

Bell, J. S., and D. I. Gough (1979), Northeast-southwest compressive stress in Alberta: Evidence from oil wells, *Earth Planet. Sci. Lett.*, *45*, 475–482, doi:10.1016/0012-821X(79)90146-8.

Benz, T., and R. Schwab (2008), A quantitative comparison of six rock failure criteria, *Int. J. Rock Mech. Min. Sci.*, *45*(7), 1176–1186, doi:10.1016/j.ijrmms.2008.01.007.

Bilotti, F., and J. H. Shaw (2005), Deep-water Niger Delta fold and thrust belt modeled as a critical-taper wedge: The influence of elevated basal fluid pressure on structural styles, *AAPG Bull.*, *89*(11), 1475–1491, doi:10.1306/06130505002.

Brudy, M., and M. D. Zoback (1999), Drilling-induced tensile wall-fractures: Implications for determination of in-situ stress orientation and magnitude, *Int. J. Rock Mech. Min. Sci.*, *36*, 191–215, doi:10.1016/S0148-9062(98)00182-X.

Brudy, M., M. D. Zoback, K. Fuchs, F. Rummel, and J. Baumgärtner (1997), Estimation of the complete stress tensor to 8 km depth in the KTB scientific drill holes: Implications for crustal strength, *J. Geophys. Res.*, *102*, 18,453–18,475, doi:10.1029/96JB02942.

Byrne, T. B., et al. (2009), Anelastic strain recovery reveals extension across SW Japan subduction zone, *Geophys. Res. Lett.*, *36*, L23310, doi:10.1029/2009GL040749.

Cai, Y., C.-Y. Wang, W.-T. Hwang, and G. R. Cochrane (1995), The effect of fault-bend folding on seismic velocity in the marginal ridge of accretionary prisms, *Pure Appl. Geophys.*, *145*, 637–646, doi:10.1007/BF00879593.

Carmichael, R. S. (1982), *Handbook of Physical Properties of Rocks*, vol. II, CRC Press, Boca Raton, Fla.

Chang, C., and B. Haimson (2000), True triaxial strength and deformability of the German Continental Deep Drilling Program (KTB) deep hole amphibolites, *J. Geophys. Res.*, *105*, 18,999–19,013, doi:10.1029/2000JB900184.

Chang, C., M. D. Zoback, and A. Khaksar (2006), Empirical relations between rock strength and physical properties in sedimentary rocks, *J. Petrol. Sci. Eng.*, *51*, 223–237, doi:10.1016/j.petrol.2006.01.003.

Colmenares, L. B., and M. D. Zoback (2002), A statistical evaluation of intact rock failure criteria constrained by polyaxial test data for five different rocks, *Int. J. Rock Mech. Min. Sci.*, *39*, 695–729, doi:10.1016/S1365-1609(02)00048-5.

Cook, A. E., D. Goldberg, and R. L. Kleinberg (2008), Fracture-controlled gas hydrate systems in the northern Gulf of Mexico, *Mar. Pet. Geol.*, *25*, 932–941, doi:10.1016/j.marpetgeo.2008.01.013.

Dahlen, F. A., J. Suppe, and D. Davis (1984), Mechanics of fold-and-thrust belts and accretionary wedges: Cohesive Coulomb theory, *J. Geophys. Res.*, *89*, 10,087–10,101, doi:10.1029/JB089iB12p10087.

Davis, D., J. Suppe, and F. A. Dahlen (1983), Mechanics of fold-and-thrust belts and accretionary wedges, *J. Geophys. Res.*, *88*, 1153–1172, doi:10.1029/JB088iB02p01153.

Goldberg, D., et al. (2003), Stress orientation and constraints on the magnitudes of in situ strength of hydrate bearing sediments: Evidence from borehole breakouts at ODP leg 204 Sites, Hydrate Ridge, *Eos Trans. AGU*, *84*(46), Fall Meet. Suppl., Abstract OS51C-0874.

Haimson, B., and C. Chang (2002), True triaxial strength of the KTB amphibolite under borehole wall conditions and its use to estimate the maximum horizontal in situ stress, *J. Geophys. Res.*, *107*(B10), 2257, doi:10.1029/2001JB000647.

Haimson, B. C., and C. G. Herrick (1985), In situ stress evaluation borehole breakouts-experimental studies, in *Proceedings of the 26th U. S. Symposium on Rock Mechanics*, edited by E. Ashworth, pp. 1207–1218, A. A. Balkema, Rotterdam, Netherlands.

Haimson, B. C., and C. G. Herrick (1986), Borehole breakouts—A new tool for estimating in situ stress?, paper presented at International Symposium on Rock Stress Measurements, Lulea Univ. of Technol., Stockholm.

Heidbach, O., et al. (2008), The World Stress Map database release, doi:10.1594/GFZ.WSM.Rel2008, Helmholtz Cent. Potsdam, GFZ Ger. Res. Cent. for Geosci., Potsdam, Germany.

Heidbach, O., et al. (2010), Global crustal stress pattern based on the 2008 World Stress Map database release, *Tectonophysics*, *482*, 3–15, doi:10.1016/j.tecto.2009.07.023.

Horsrud, P. (2001), Estimating mechanical properties of shale from empirical correlations, *SPE Drill. Completion*, *16*, 68–73.

Ienaga, M., et al. (2006), Borehole image analysis of the Nankai Accretionary Wedge, ODP Leg 196: Structural and stress studies, *Tectonophysics*, *426*, 207–220, doi:10.1016/j.tecto.2006.02.018.

Ito, Y., Y. Asano, and K. Obara (2009), Very-low-frequency earthquakes indicate a transpressional stress regime in the Nankai accretionary prism, *Geophys. Res. Lett.*, *36*, L20309, doi:10.1029/2009GL039332.

Jaeger, J. C., N. G. W. Cook, and R. W. Zimmerman (2007), *Fundamentals of Rock Mechanics*, 4th ed., Blackwell, Malden, Mass.

King, R. C., et al. (2010), Present-day stresses in Brunei, NW Borneo: Superposition of deltaic and active margin

tectonics, *Basin Res.*, *22*, 236–247, doi:10.1111/j.1365-2117.2009.00407.x.

Kopf, A., and K. M. Brown (2003), Friction experiments on saturated sediments and their implications for the stress state of the Nankai and Barbados subduction thrusts, *Mar. Geol.*, *202*, 193–210, doi:10.1016/S0025-3227(03)00286-X.

Kukowski, N., et al. (2002), Mechanical decoupling and basal duplex formation observed in sandbox experiments with application to the Western Mediterranean Ridge accretionary complex, *Mar. Geol.*, *186*, 29–42, doi:10.1016/S0025-3227(02)00171-8.

Lal, M. (1999), Shale stability: Drilling fluid interaction and shale strength, paper presented at Latin American and Caribbean Petroleum Engineering Conference, Soc. of Pet. Eng., Caracas, Venezuela.

Lama, R. D., and V. S. Vutukuri (1978), *Handbook on Mechanical Properties of Rocks*, vol. II, Trans Tech., Clausthal, Germany.

Lin, W., et al. (2010), Present-day principal horizontal stress orientations in the Kumano forearc basin of the southwest Japan subduction zone determined from IODP NanTroSEIZE drilling Site C0009, *Geophys. Res. Lett.*, *37*, L13303, doi:10.1029/2010GL043158.

Martin, K. M., S. P. S. Gulick, N. L. B. Bangs, G. F. Moore, J. Ashi, J.-O. Park, S. Kuramoto, and A. Taira (2010), Possible strain partitioning structure between the Kumano fore-arc basin and the slope of the Nankai Trough accretionary prism, *Geochem. Geophys. Geosyst.*, *11*, Q0AD02, doi:10.1029/2009GC002668.

Mastin, L. G. (1984), Development of borehole breakouts in sandstone, M.S. thesis, Stanford Univ., Palo Alto, Calif.

Mouchet, J. P., and A. Mitchell (1989), *Abnormal Pressures While Drilling*, Elf Aquitaine, Boussens, France.

Saffer, D., L. McNeill, E. Araki, T. Byrne, N. Eguchi, S. Toczko, K. Takahashi, and the Expedition 319 Scientists (2009), *NanTroSEIZE Stage 2: NanTroSEIZE Riser/Riserless Observatory*, *Integrated Ocean Drill. Program Prelim. Rep.*, vol. 319, doi:10.2204/iodp.pr.319.2009, Integrated Ocean Drill. Program, Washington, D. C.

Sassi, W., and J.-L. Faure (1996), Role of faults and layer interfaces on the spatial variation of stress regimes in basins: Inferences from numerical modeling, *Tectonophysics*, *266*, 101–119, doi:10.1016/S0040-1951(96)00185-0.

Sawyer, A. H., P. Flemings, D. Elsworth, and M. Kinoshita (2008), Response of submarine hydrologic monitoring instruments to formation pressure changes: Theory and application to Nankai advanced CORKs, *J. Geophys. Res.*, *113*, B01102, doi:10.1029/2007JB005132.

Scholz, C. H. (1990), *The Mechanics of Earthquakes and Faulting*, Cambridge Univ. Press, New York.

Seno, T., S. Stein, and A. E. Gripp (1993), A model for the motion of the Philippine Sea plate consistent with NUVEL-1 and geological data, *J. Geophys. Res.*, *98*, 17,941–17,948, doi:10.1029/93JB00782.

Seyferth, M., and A. Henk (2000), Deformation, metamorphism and exhumation: Quantitative models for a continental collision zone in the Variscides, in *Orogenic Processes: Quantification and Modelling in the Variscan Belt*, edited by W. Franke et al., *Geological Society Spec. Publ.*, *179*, 217–230.

Shen, B. (2008), Borehole breakouts and in situ stress, in *SHIRMS*, edited by Y. Potvin et al., pp. 407–418, Aust. Cent. for Geomech., Perth, West. Aust., Australia.

Suppe, J. (2007), Absolute fault and crustal strength from wedge tapers, *Geology*, *35*, 1127–1130, doi:10.1130/G24053A.1.

Tingay, M., et al. (2005), Understanding tectonic stress in the oil patch: The World Stress Map Project, *Leading Edge*, *24*, 1276–1282, doi:10.1190/1.2149653.

Tingay, M., J. Reinecker, and B. Mueller (2008), Borehole breakout and drilling-induced fracture analysis from image logs [online], in *World Stress Map Project—Guidelines: Image Logs*, Helmholtz Cent. Potsdam, GFZ Ger. Res. Cent. for Geosci., Potsdam, Germany. (Available at http://dc-app3-14.gfz-potsdam.de/pub/guidelines/WSM_analysis_guideline_breakout_image.pdf)

Tingay, M. R. P., et al. (2009), Present-day stress and neotectonics of Brunei: Implications for petroleum exploration and production, *AAPG Bull.*, *93*(1), 75–100, doi:10.1306/08080808031.

Tobin, H., M. Kinoshita, K. T. Moe, and the Expedition 314 Scientists (2009), Expedition 314 summary [online], *Proc. Integrated Ocean Drill. Program, 314/315/316*, 42 pp., doi:10.2204/iodp.proc.314315316.111.2009. (Available at http://publications.iodp.org/proceedings/314_315_316/111/111_.htm)

Vernik, L., and M. D. Zoback (1992), Estimation of maximum horizontal principal stress magnitude from stress-induced well bore breakouts in the Cajon Pass scientific research borehole, *J. Geophys. Res.*, *97*, 5109–5119, doi:10.1029/91JB01673.

Wang, K. (2000), Stress-strain 'paradox', plate coupling, and forearc seismicity at the Cascadia and Nankai subduction zones, *Tectonophysics*, *319*, 321–338, doi:10.1016/S0040-1951(99)00301-7.

Wang, K., and J. He (1999), Mechanics of low-stress forearcs: Nankai and Cascadia, *J. Geophys. Res.*, *104*, 15,191–15,205, doi:10.1029/1999JB900103.

Wang, K., and Y. Hu (2006), Accretionary prisms in subduction earthquake cycles: The theory of dynamic Coulomb wedge, *J. Geophys. Res.*, *111*, B06410, doi:10.1029/2005JB004094.

Wang, K., and K. Suyehiro (1999), How does plate coupling affect crustal stresses in northeast and southwest Japan?, *Geophys. Res. Lett.*, *26*(15), 2307–2310, doi:10.1029/1999GL900528.

Willett, S. D. (1999), Rheological dependence of extension in wedge models of convergent orogens, *Tectonophysics*, *305*(4), 419–435, doi:10.1016/S0040-1951(99)00034-7.

Xu, J., and Y. Kono (2002), Geometry of slab, intraslab stress field and its tectonic implication in the Nankai trough, Japan, *Earth Planets Space*, *54*, 733–742.

Zhao, S., et al. (2003), Deformation and stress localization at the Nankai subduction zone, southwest Japan, *Earth Planet. Sci. Lett.*, *206*, 145–160, doi:10.1016/S0012-821X(02)01073-7.

Zhao, W. L., et al. (1986), Origin of convex accretionary wedges: Evidence from Barbados, *J. Geophys. Res.*, *91*, 10,246–10,258, doi:10.1029/JB091iB10p10246.

Zhou, S. (1994), A program to model the initial shape and extent of borehole breakout, *Comput. Geosci.*, *20*, 1143–1160, doi:10.1016/0098-3004(94)90068-X.

Zoback, M. L. (1992), First- and second-order patterns of stress in the lithosphere: The world stress map project, *J. Geophys. Res.*, *97*, 11,703–11,728, doi:10.1029/92JB00132.

Zoback, M. D. (2007), *Reservoir Geomechanics*, doi:10.1017/CBO9780511586477, Cambridge Univ. Press, New York.